JOURNAL OF GEOPHYSICAL RESEARCH: SPACE PHYSICS, VOL. 118, 2419–2427, doi:10.1002/jgra.50244, 2013

Large-scale ionospheric disturbances due to the dissipation of convectively-generated gravity waves over Brazil

H.-L. Liu[1] and S. L. Vadas[2]

Received 4 September 2012; revised 21 March 2013; accepted 22 March 2013; published 9 May 2013.

[1] In a companion paper, we show that large-scale secondary gravity waves and circulation cells are created by the body forces generated by the dissipation of convectively generated gravity waves over Brazil on 01 October 2005. In this paper, we show that these fluid perturbations cause large-scale perturbations of the plasma drift and plasma density in the ionosphere by changing the wind dynamo and transport. These fluid perturbations modify both the amplitude and direction of the plasma drifts. Near the geomagnetic equator, the magnitude of the pre-reversal enhancement can be increased or weakened, depending on the location and local time. Because the circulation cells persist from late afternoon through midnight, the modulation of the vertical drift near the geomagnetic equator persists until midnight. The largest changes of the wind-driven currents can occur either in the E or F region and are determined by the magnitudes of the wind perturbations, conductivities, and conductivity perturbations. The contributions to the plasma transport changes are from advection by the neutral winds along field lines, plasma drifts, and ambipolar diffusion, in the order of their relative significance in the numerical results.

Citation: Liu, H.-L., and S. L. Vadas (2013), Large-scale ionospheric disturbances due to the dissipation of convectively-generated gravity waves over Brazil, *J. Geophys. Res. Space Physics*, *118*, 2419–2427, doi:10.1002/jgra.50244.

1. Introduction

[2] Atmospheric gravity waves (GWs) are thought to be one possible cause of traveling ionospheric disturbances (TIDs) [*Hocke and Schlegel*, 1996; *Klostermeyer*, 1972], which may seed equatorial spread F (ESF). This possible connection was a key motivation of the Spread F Experiment (SpreadFEx) campaign [*Fritts et al.*, 2009, and references therein]. The observations during the campaign suggested that the presence of precursor gravity waves of detectable intensity is a necessary condition for spread F instability initiation when the vertical drift is less than 20 ms^{-1} [*Abdu et al.*, 2009]. The sources of the GWs in the thermosphere are most often associated with the upward propagation of waves excited in the troposphere by convection, orography, adjustment of unbalanced flows, wind shear and wave-wave interactions [e.g., *Fritts and Alexander*, 2003], and wave generation within the thermosphere/ionosphere by Joule heating and/or Lorentz force in the auroral region [*Richmond*, 1978]. TIDs have also been tied to internal gravity waves excited by tsunami [e.g., *Artru et al.*, 2005; *DasGupta et al.*, 2006; *Liu et al.*, 2006b, 2006a; *Lognonné et al.*, 2006; *Occhipinti et al.*, 2006, 2011]. The GWs that propagate from the lower atmosphere dissipate and deposit their momentum when they either become unstable due to their exponential growth with altitude or encounter increasingly strong molecular dissipation in the thermosphere. Recent theoretical studies have shown that the forcing exerted by wave dissipation (dubbed thermospheric body forces) can generate secondary GWs, some of which can propagate in the thermosphere/ionosphere [*Vadas and Fritts*, 2001; *Vadas*, 2007, and references therein].

[3] Observational evidence of secondary GWs from thermospheric body forces are suggested by two recent studies. *Bruinsma and Forbes* [2008] observed the quiet-time neutral density perturbations at z = 400 km with the CHAMP satellite and found significant local time variations on horizontal scales between 160 and 2400 km. The perturbations associated with the largest scales were found to be consistent with secondary GWs from deep convection [*Vadas and Liu*, 2009]. Only GWs with intrinsic phase speeds greater than ∼350–400 m/s can reach such altitude when wave damping by molecular viscosity is taken into account[*Vadas*, 2007]. Because GWs with phase speeds greater than ∼280–300 ms^{-1} cannot propagate in the lower atmosphere [*Vadas and Crowley*, 2010], these GWs must have been excited in the thermosphere. *Vadas and Crowley* [2010] detected TIDs at the bottomside of the F layer, which were propagating northwest and northward, from the direction of Tropical Storm (TS) Noel. This storm was ∼1700–2000 km south and southeast of the observation location. They found that 40% had phase speeds larger than 280 m/s, indicative

[1]High Altitude Observatory, National Center for Atmospheric Research, Boulder, Colorado, USA.
[2]NorthWest Research Associates, Boulder, Colorado, USA.

Corresponding author: H.-L. Liu, High Altitude Observatory, National Center for Atmospheric Research P.O.Box 3000, Boulder, CO 80307-3000, USA. (liuh@ucar.edu)

2169-9380/13/10.1002/jgra.50244

of a thermospheric (not tropospheric) source. Using reverse ray tracing, they determined that most of the observed GWs were likely secondary GWs generated by the thermospheric body forces created from the dissipation of primary GWs excited by deep convection within TS Noel. These identified secondary GWs had horizontal wavelengths of $\sim$ 100 to several thousand kilometers and periods of 10 min to several hours.

[4] Numerical experiments using the National Center for Atmospheric Research (NCAR) thermosphere-ionosphere-mesosphere-electrodynamics general circulation model (TIME-GCM), with a body force modeled after the dissipation of GWs from a single tropical convective plume during the SpreadFEx campaign, demonstrated that large-scale (horizontal scale larger than 1000 km) globally-propagating GWs are excited by this body force [*Vadas and Liu*, 2009]. These large-scale GWs had horizontal wavelengths of $\sim$2000 km and phase speeds of $\sim$500 m/s. They also showed that large-amplitude, large-scale circulation cells are created by this force. Finally, they showed that this force created large perturbations in the total electron content (TEC). Thus, they demonstrated that the dissipation of GWs excited by a single, deep convective plume can create large-amplitude, large-scale variability in the neutral winds, temperature, and density, and in the TEC.

[5] In our companion paper, the previous study was generalized to calculate the thermospheric body forces as a function of (x, y, z, t) from hundreds of convective plumes that occurred over a 6 h period and in a $20° \times 20°$ region for the same evening as in the previous study [*Vadas and Liu*, 2013]. These body forces were then interpolated into the NCAR TIME-GCM. The characteristics of the primary and secondary GWs, the generated circulation cells, and the neutral temperature and density changes were discussed in detail. Additionally, the plasma responses (e.g., TEC) were also examined briefly.

[6] The objective of this study is to investigate the large-scale ionospheric impacts of these generated fluid perturbations. In particular, we examine the ionospheric plasma density, vertical component of $\mathbf{E} \times \mathbf{B}$ drift (referred to as vertical drift hereafter), electric conductivities, and transport. It is expected that the neutral wind perturbations from these body forces can change the plasma density and electric conductivities by changing the transport, and that the perturbations in both the winds and conductivities can in turn modulate the ionospheric electric field and plasma drift through the wind dynamo. Because the plasma vertical drift, especially the pre-reversal enhancement (PRE) of the vertical drift after sunset, may play a key role in the generation of ESF [e.g., *Fejer et al.*, 1999; *Anderson et al.*, 2004], it is valuable to understand the variability of the vertical drift due to the large-scale fluid perturbations from deep tropospheric convection. Recent observations of ionospheric drift and density perturbations with spatial scales of 500–1000 km under extreme solar minimum conditions [*Pfaff et al.*, 2010] provide another motivation for this work.

[7] Brief descriptions of the ray-tracing model, the NCAR TIME-GCM and setup of numerical experiments are given in section 2. Analysis of simulation results are presented in section 3, followed by a discussion and conclusions in sections 4 and 5.

2. Numerical Models

[8] For this study, the primary GWs excited by all convective plumes that overshooted the tropopause within a $20° \times 20°$ region in central Brazil, 45 – 65°W and 0 – 20°S were modeled during 6 h in the evening of 01 October 2005. GOES satellite infrared (IR) images every 30 min from 1822 to 2353 UT were used to determine the parameters of those convective plumes overshooting the tropopause [*Vadas and Liu*, 2013]. Deep convection peaked at 19–22 UT and weakened rapidly after 23 UT. 136 convective objects are identified from the images. The average plume diameter in each object ranges from 5 to 20 km. The plume updraft velocities are estimated from Convective Available Potential Energy (CAPE) maps [*Vadas and Liu*, 2009; *Vadas and Crowley*, 2010], and range from 0 to 63 ms^{-1}. In this study, only those objects with updraft velocities larger than 10 ms^{-1} are selected.

[9] Each convective plume was modeled as a vertical body force [*Vadas and Fritts*, 2009], and then the excited GWs were ray traced into the thermosphere using background winds and temperatures from the TIME-GCM and radar observations [*Vadas and Liu*, 2009]. The GW fields were reconstructed as described in *Vadas and Fritts* [2009], and the Reynolds stress momentum flux divergence was then calculated. We now also include the effects of parameterized wave breaking [*Lindzen*, 1981]. These thermospheric body forces were then inputted into the TIME-GCM using temporal and spatial interpolation [*Vadas and Liu*, 2013]. Detailed description of the convective sources, the generation, propagation and dissipation of the gravity waves, and the thermospheric responses are also presented in *Vadas and Liu* [2013].

[10] The NCAR TIME-GCM simulates the circulation, temperature, and compositional structures of the upper atmosphere (30–500 km) and the ionosphere, and it includes the dynamical, chemical, and electrodynamical processes in that atmospheric region. Details of the model can be found in *Roble and Ridley* [1994]; *Roble* [1995; 2000, and references therein]. The model spatial resolution used is four grids/scale height and $2.5° \times 2.5°$ in vertical and horizontal directions, respectively, with forcing at the lower boundary specified by the European Centre for Medium-Range Weather Forecast reanalysis data for the campaign time period. TIME-GCM simulations were conducted without and with the thermospheric body forces.

3. Results

[11] As shown in *Vadas and Liu* [2013, Figure 10], the body forces exerted by the dissipation of gravity waves occur between 120 and 220 km. To avoid double counting, the GW forces from the ray tracing model are smoothly zeroed out below 120 km. The GWs generated by the body forces cause large ionospheric perturbations in electric field/plasma drift, as determined by comparing the TIME-GCM simulations with and without the body forces (Figure 1). The perturbation of the vertical drift at the equator starts at $\sim$1900 UT between 50°W and 60°W, the longitudes where the body forces occur persists for more than 10 h and shows clear signatures of global propagation. For example, the phase speed of the fast eastward branch with upward vertical drift perturbations is about

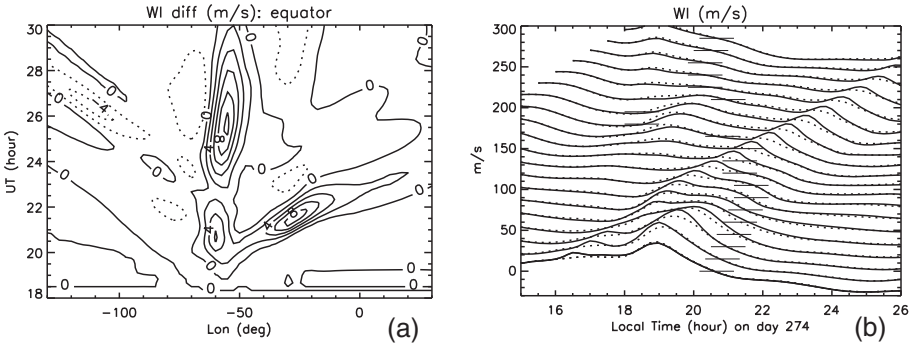

Figure 1. (a) Changes of plasma drift in the vertical direction (plotted at the geographic equator at ∼170 km). Contour interval: 2 ms^{-1} (solid line: upward). These changes are approximately independent of altitude. (b) Total vertical drift at the geographic equator from the TIME-GCM simulations with the body forces (solid) and without the body forces (dotted) every half hour between 2030 and 0600 UT (shifted upward by 20 ms^{-1} for each half hour). The thin horizontal lines indicate the zero values for the respective drift profiles.

570 ms^{-1}, and perturbations encompass ∼80° in longitude. The almost stationary branch between 50°W and 60°W corresponds to recurring body forces there between 1900 and 2200 UT, which can be traced back to the deep convective systems over Brazil for that night as described in the previous section. The largest changes of the vertical drift on these two branches are upward and between 8 and 10 ms^{-1}, located around ∼25°W/2130 UT and ∼55°W/0130 UT. The local times corresponding to those changes are ∼1950 LT and 2150 LT, respectively. Figure 1b shows the total vertical drift every half hour between 2030 and 0600 UT of the following day from the case with the GW body forces (solid line) and that without (dotted line). In Figure 1b, we have converted longitude into local time and made the plot in local time coordinate for easy interpretation. We also indicate where the vertical drifts are zero via short horizontal lines. The pre-reversal enhancement (PRE) is strongest at longitudes between 7.5°W and 45°W (corresponding to 2030–2200 UT for 1900–2000 UT), with a maximum of ∼ 30 m/s. It becomes stronger by ∼ 10 m/s at the geographic equator in the case with body force. Further, the nearly stationary (in longitude) branch of the upward vertical drift perturbation persists until midnight, and the total vertical drift created are sometimes comparable to PRE, but at times well after sunset.

[12] Wave structures are also reflected in TECs, which may increase or decrease depending on the phase of the wave. Figure 2 shows the percentage TEC changes. At the equator, TEC decreases are most prominent after ∼1900 UT at two longitude sectors. At around 30°W in a eastward branch of the GWs, the TEC decreases by more than 20% at 2200 UT (2000 LT). At ∼50°W and 0200 UT (2240 LT), the TEC decrease exceeds 50%, and continues till after 0500 UT (0140 LT). The magnitude of the relative TEC change before sunset in the simulation is about 10–20%. The wave pattern of the TEC perturbation is also seen from the map of TEC change at 0100 UT: TEC decreases up to 40% occur around the equator and 45°S, and TEC increases are seen around 60°S, 20°S, and 10°N with amplitudes of 10%, 60%, and 30%, respectively

[13] Figures 3a and 3b are longitude-height plots of the neutral wind perturbations at the geographic equator and 0100 UT, obtained by subtracting the TIME-GCM simulation without the body forces from that with it. It is seen that the wind perturbations extend from ∼110 km to the upper thermosphere, and the largest wind perturbations are found between 130 and 200 km. The large winds at z = 130–200 km are due primarily to the circulation cells created by the body forces and secondarily to the smaller wind perturbations associated with the secondary GWs [*Vadas and*

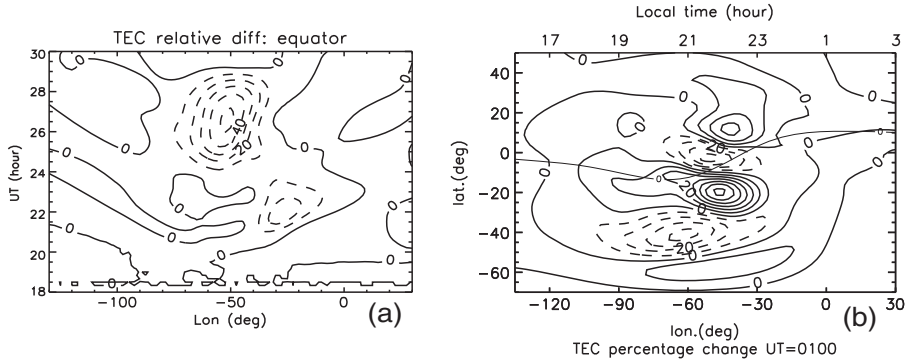

Figure 2. Relative change of the total electron content (a) at the geographic equator, and (b) at 0100 UT due to the GWs and circulation cells generated by the body forces. Contour interval 10% (solid line: increase). The thin contour line denotes the magnetic equator.

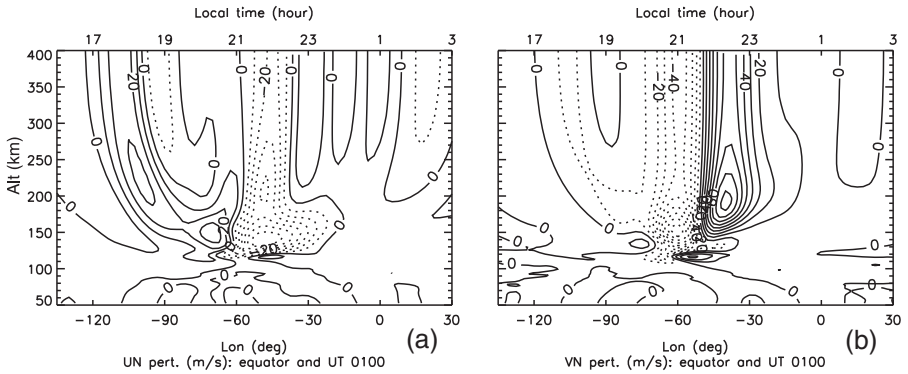

Figure 3. Neutral (a) zonal and (b) meridional wind changes at the geographic equator and 0100 UT due to gravity waves generated by the body forces. Contour interval: 10 ms^{-1} (solid line: Figure 3a, eastward; Figure 3b, northward).

Liu, 2013]. The peak wind altitudes are determined by the location of the body forces. The amplitudes of the winds within the circulation cells decay with distance above this peak altitude. Many of the larger-scale secondary GWs are able to propagate up to z = 375 km because their amplitudes are approximately constant with altitude, even though the neutral density decreases exponentially with altitude, this indicates that the GWs are partially dissipating with altitude. This occurs because the molecular viscosity increases exponentially with altitude.

[14] Because the wind perturbations encompass the ionospheric E and F regions, they modulate the ionosphere through the E and F region dynamo. Figure 4a shows the vertical profiles of Hall and Pedersen conductivities (σ_H and σ_P, respectively) at 45°W, near the magnetic equator and at 0100 UT (2200 LT for that location) from the two TIME-GCM simulations. At this location, both σ_H and σ_P increase in the F-region, reflecting increase of plasma density therein (discussed later). A map of σ_P perturbation on pressure level 1.6×10^{-7} hPa (near the F2 peak) at 0100 UT (Figure 4b) displays a clear wave modulation, and the magnitude (about 10^{-5} Sm^{-1}) is large compared with the unperturbed values.

[15] The wind driven Pedersen and Hall currents, $\vec{J}_P^W$ and $\vec{J}_H^W$, perpendicular to field lines in the ionosphere are proportional to Pedersen and Hall conductivities and wind velocities,

$$\vec{J}_P^W = \sigma_P \vec{U} \times \vec{B} \quad (1)$$

$$\vec{J}_H^W = -\sigma_H(\vec{U} \times \vec{B}) \times \vec{b} \quad (2)$$

where $\vec{U}$ is the neutral wind, and $\vec{b}$ the unit vector in the direction geomagnetic field $\vec{B}$. The polarized electric field is determined by the integration of these currents along the field lines. Therefore, the perturbations of the electric field and plasma drift have a complex dependence on the wind perturbations at different latitudes, longitudes, and heights, and in particular at the E region heights where σ_H and F region heights where σ_P peaks.

[16] To further examine this dependence, although still in a qualitative fashion, we show the altitudes where the wind driven current perturbations maximize (the horizontal components of $\vec{J}_P^W$ and $\vec{J}_H^W$) and their dependence on latitude and longitude/local time (Figure 5). Overplotted is the perturbation of the vertical plasma drift obtained from TIME-GCM. At the plotted UT time (0100 UT), the largest perturbation of

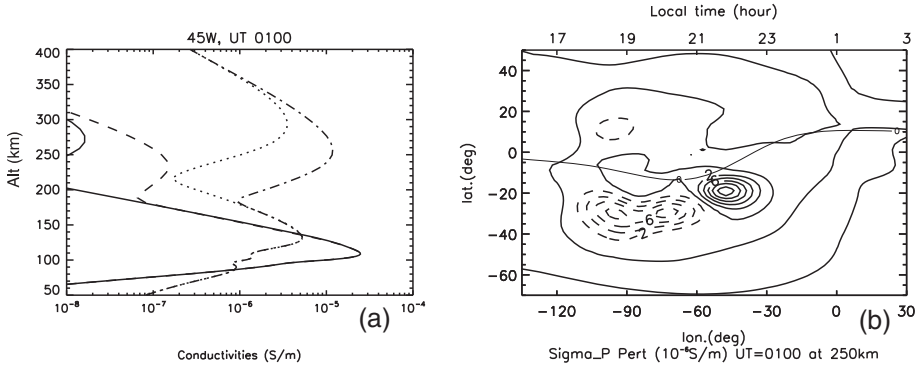

Figure 4. (a) Hall (solid and dashed lines) and Pedersen (dotted and dash-dotted lines) conductivities at 45°W and 0100 UT near the magnetic equator from TIME-GCM simulation without the body forces (solid and dotted lines) and with the body forces (dashed and dash-dotted lines). (b) Changes of F-region Pedersen conductivity at pressure level 1.6×10^{-7} hPa (~250 km) and 0100 UT. Contour interval: 10^{-6} Sm^{-1} (solid line: increase). The thin contour line in Figure 4b denotes the magnetic equator.

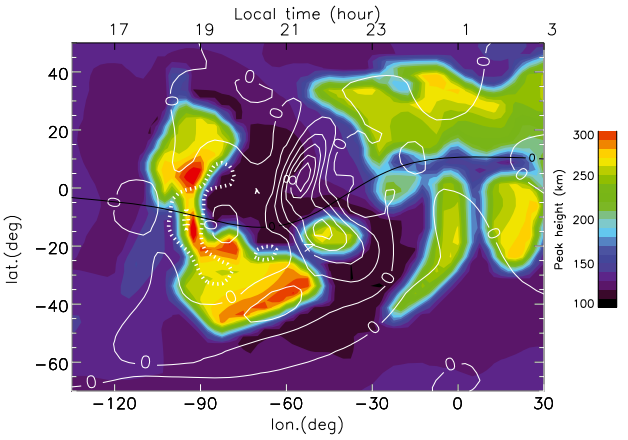

Figure 5. Height (in km) where the difference between the wind driven current with and without the body forces maximizes in either zonal or meridional direction at 0100 UT (colored, shaded contour). The overplotted white line contour is the change of the vertical plasma drift. Contour interval: 2 ms^{-1} (solid line: upward, dotted line: downward). The thin black contour line denotes the magnetic equator.

the vertical plasma drift is found between 30°W and 70°W (LT 2030–2300), with the two peaks of 8–10 ms^{-1} flanking the magnetic equator. The longitudes/local times of the maximum drift perturbation are consistent with those of the maximum wind perturbations, as shown in Figure 3. The altitudes with the largest wind driven currents vary between E and F regions. In general, the currents peak in the E region near the locations of the body forces (GW source region) and in the F region further away from the source. This roughly follows the cone/ring pattern of the GW propagation in the vertical/horizontal direction, with the radius of the phase front of the wave (the ring) increasing with altitude (Figure 6), as dictated by the wave dispersion relation. However, this ring structure is not as clearly defined in Figure 5 as the ring pattern in the temperature or neutral wind perturbations (the latter are shown in *Vadas and Liu* [2013]). This is because apart from the neutral winds, the currents are also dependent on the conductivities, which vary with latitude, longitude/local time, and integrated over altitude. Further, it is seen from Figure 4 that the Pedersen and Hall conductivities can be strongly modified in the F region, as a result of plasma density perturbation. When compounded with wind changes, this will introduce nonlinear changes to the total currents.

[17] From Figure 6, it is seen that the zonal wind perturbations at 60°W and the magnetic equator are 50 and 80 ms^{-1} at E and F altitudes, respectively. The E region Hall and F region Pedersen conductivities at the same location are 2.3×10^{-5} and 2.5×10^{-6} Sm^{-1}, respectively. Therefore, the zonal component of $\vec{J}_H^W$ in the E region is stronger than the meridional component of $\vec{J}_P^W$ in the F region (meridional and zonal components of the two currents are 0 at the magnetic equator). At 45°W and 15°S, on the other hand, the Pedersen conductivity increases significantly, similar to that demonstrated in Figure 4. The E and F region zonal wind perturbations there are 20 and 80 ms^{-1} (meridional wind perturbations 0 and 80 ms^{-1}, not shown) respectively. As a result, the largest wind driven current there is in the F region. At higher geomagnetic latitudes, the largest wind driven current perturbations are found in the E region, even though the wind perturbations are stronger in the F region. This is because the nighttime F region Pedersen conductivity in the model displays a latitudinal dependence and decreases rapidly poleward of ∼10-15° magnetic latitudes, while the E region Hall conductivity does not vary as much with latitude.

[18] The variation of the altitudes with maximum wind driven current perturbations demonstrates the complex and dynamic nature of the ionospheric response to the GWs. The actual changes of the electric field and plasma drift are dependent on the spatial gradients of these currents, their integration along the field lines, and the interplay of the E and F region dynamo. These processes are captured by the TIME-GCM [*Richmond et al.*, 1992], and a more detailed diagnostic analysis will be performed to understand them in future studies.

[19] The transport of the ion densities (dominantly O^+ near the F region peak) is determined by the neutral winds, plasma drifts, and ambipolar diffusion

$$\left(\frac{\partial n_{O^+}}{\partial t}\right)_{\text{trans}} = -\nabla\cdot(n_{O^+}\vec{V}) \tag{3}$$

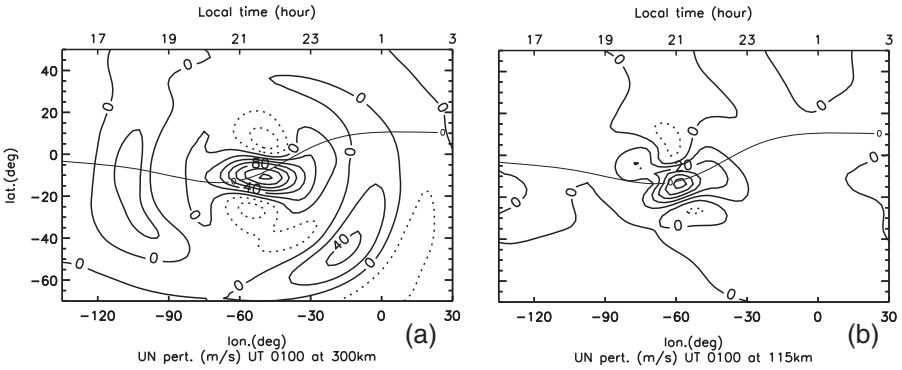

Figure 6. Neutral zonal wind changes at (a) ∼300 km and (b) ∼115 km and 0100 UT due to gravity waves generated by the body forces. Contour intervals are 20 ms^{-1} (Figure 6a) and 10 ms^{-1} (Figure 6b) (solid line: eastward). The thin contour line denotes the magnetic equator.

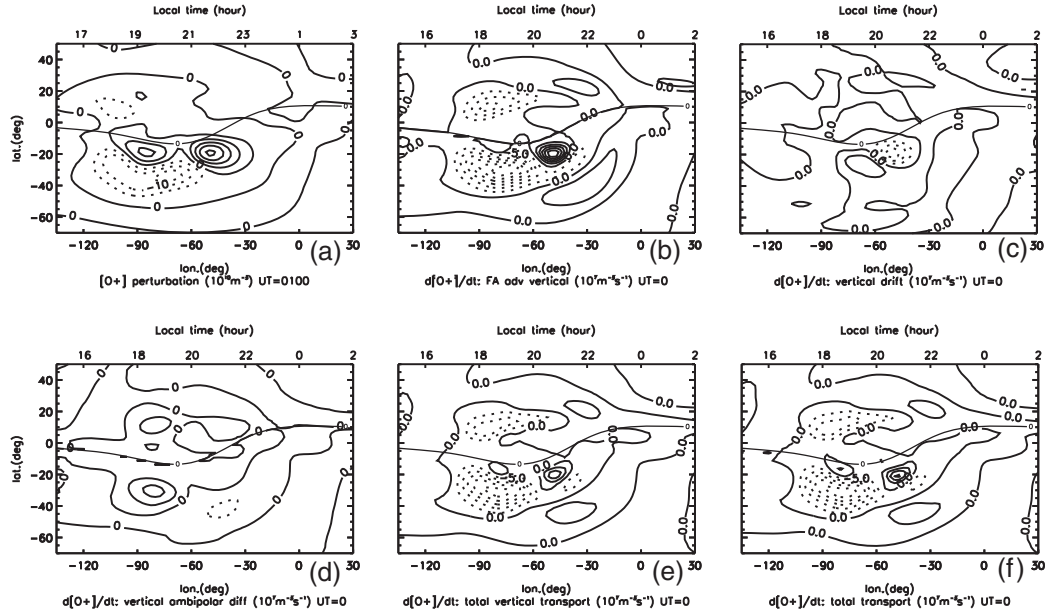

Figure 7. (a) The change of O^+ number density due to gravity waves generated by the body forces about one scale height below the F peak at 0100 UT. Contour interval: 5×10^{10}m^{-3} (solid line: increase). The change of the [O^+] tendency due to gravity waves associated with the divergence of the vertical component of (b) the field-aligned advection by neutral wind, (c) the transport by plasma drift, and (d) the ambipolar diffusion. Figure 7e is the sum of Figures 7b–7c, and Figure 7f is the change of total [O^+] tendency due to transport. Figures 7b–7f are at the same altitude as Figure 7a and 0 UT. Contour interval: Figures 7b–7c and Figures 7e–7f: 2.5×10^7 m^{-3}s^{-1}; Figure 7d: 10^7 m^{-3}s^{-1} (solid line: increase). The thin contour line denotes the magnetic equator.

$$\vec{V} = \vec{V}_{\parallel} + \vec{V}_{\perp} \tag{4}$$

$$\vec{V}_{\parallel} = \vec{b}\cdot\left(\vec{U} + \frac{1}{\nu_{\text{in}}}\left(\vec{g} - \frac{1}{\rho_{O+}}(\nabla(p_i + p_e))\right)\right)\vec{b} \tag{5}$$

$$\vec{V}_{\perp} = \frac{\vec{E}\times\vec{B}}{|B|^2} \tag{6}$$

where n_{O+} is the O^+ number density, $\vec{V}$ the total ion transport velocity, $\vec{E}$ the electric field, $\vec{g}$ is the gravitational force, $\parallel$ and $\perp$ for directions parallel and perpendicular to the magnetic field line, respectively, ν_{in} the ion-neutral collision frequency, ρ_{O+} the O^+ mass density, and p_i and p_e the ion and electron pressure, respectively. Note that here we focus on the change of O^+ number density by transport only, which is generally dominant over the production and loss in the F region at nighttime. The first term on the right-hand side of equation 5 is the field-aligned transport by neutral wind, and the second and third terms are transport due to ambipolar diffusion, respectively. The transport in the perpendicular direction comes from the $\vec{E}\times\vec{B}$ drift (equation 6). In Figure 7, we show the O^+ perturbations for the case with the body force minus the control case (without the body force). In this figure, we project these transport terms onto the longitude and latitude at ~280 km (one scale height below the F peak). We find that the divergence of their vertical components, $\partial(\vec{V}\cdot\vec{e}_z)/\partial z$ ($\vec{e}_z$ is the unit vector in the vertical direction), are much larger than other transport terms. At 0000 UT, the vertical divergence of the field-aligned transport by neutral winds is the largest immediately beneath the F region peak, which in turn is mainly caused by the meridional wind perturbation of the GWs. The meridional wind perturbation east of 60°W and south of the magnetic equator is southward, which causes the downward transport of O^+ along the field line. This tends to lower the F peak altitude and thus increases the O^+ below the F peak. The meridional wind perturbations to the west on both sides of the magnetic equator, on the other hand, are equatorward, which push the O^+ upward along the field line, increase the F peak altitudes, and decrease O^+ below the F peak. The upward perturbation of the plasma drift east of 60°W causes the decrease of O^+. Compared with these two terms, the transport due to the vertical divergence of the ambipolar diffusion is secondary, but still much larger than divergence of the horizontal components of the other transport terms. Therefore, the total transport tendency is very close to the total vertical divergence of the transport terms.

[20] It is also evident from the figure that the perturbation of O^+ density at 0100 UT (Figure 7a) is consistent with the O^+ tendency at earlier times (0000 UT is shown in Figure 7f). The plasma density perturbations lead to changes in the electric conductivities. For example, the increases of the F region Pedersen and Hall conductivities at 45°W and 15°S (Figure 4a) are caused by the increase of plasma density at the same location (Figure 7a), and the spatial modulation of σ_P shown in Figure 4b is similar to the spatial modulation of plasma density at the same altitude. By comparing Figure 7a and Figure 7c, it is seen that the perturbations of the plasma density are not necessarily in phase with the plasma density perturbations by plasma drift. For example, between 30 and 60°W, the upward vertical drift perturbation causes a decrease in plasma density south dip

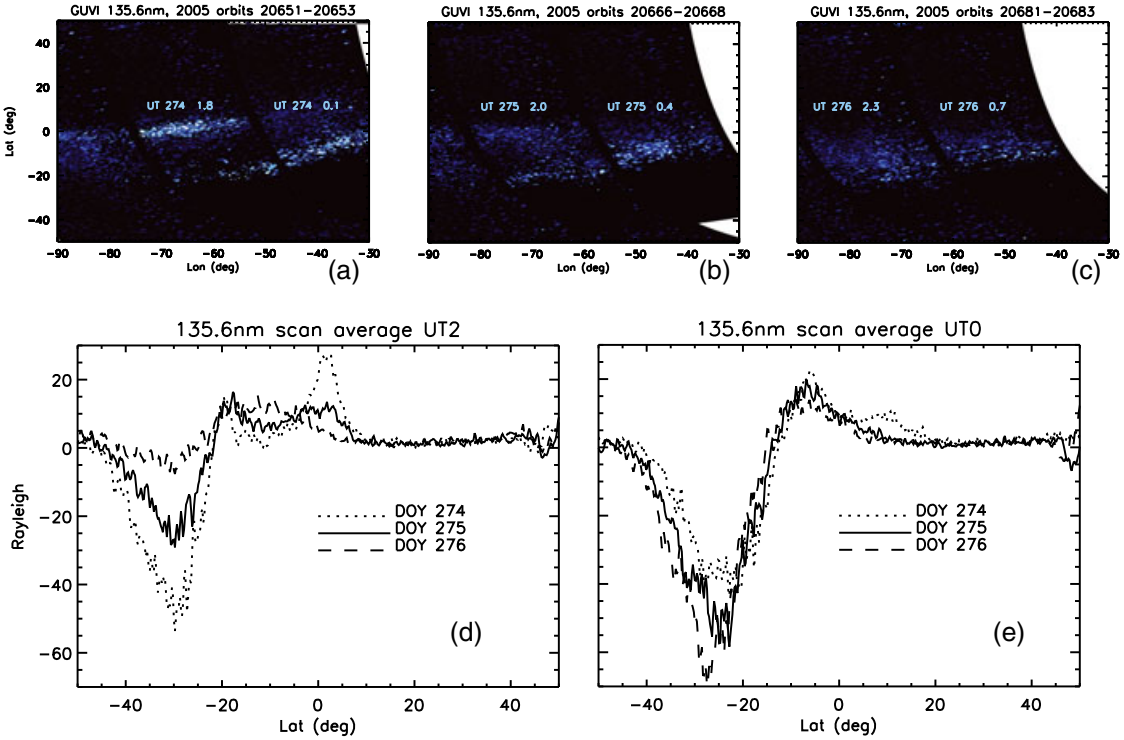

Figure 8. (a–c) GUVI measurements of night time 135.6 nm emission rates on days 274–276 of 2005. Orbits 20651–20652, 20666–20667, and 20681–20682 (in a-c respectively) cover South America at around 0 UT and 0200. The contour levels are between 0 and 40 Rayleigh. (d–e): Profiles of 135.6 nm emission rates along the satellite orbits at ∼0200 UT and 0 UT, obtained by averaging the rates over each disk scan. The negative values are likely contamination caused by the scattering of the strong Lyman-α emission.

equator at this altitude, while the total plasma density there actually increases. This is because of the dominant contribution from the advection by neutral winds along the field line, as well as the time-integrated effect of advection.

4. Discussion

[21] As mentioned in section 1, it has been suggested that the upward plasma drift due to PRE may help set up ESF. It is evident from the numerical results presented here that PRE can be modulated by the large-scale GWs and circulation cells generated indirectly by deep tropical convection (via body forces), and thus may affect the formation of bubbles. According to our results, these induced fluid perturbations can either enhance or weaken the upward vertical drift, depending on the horizontal location and local time. Furthermore, we show here that the perturbations of the plasma drift due to these body forces last well after sunset, until midnight or later, contingent on the presence of deep tropospheric convection and the longevity of the circulation cells. In the SpreadFEx observational campaign, *Kherani et al.* [2009] reported that the post-reversal vertical drift oscillates in time from sunset to midnight, with the upward drift decelerating or reversing before it became upward again. Such oscillations, especially the extension of the upward drift well after dusk, are qualitatively similar to what is seen in our simulations. They are presumably associated with GWs and may play an important role in initiating the observed F-region bubbles for the night of 5–6 October, as pointed out by *Kherani et al.* [2009]. It should be noted that the Nyquist wavelength resolvable by the model is ∼500 km in the equatorial region, so mesoscale waves (primary or secondary) or wave effects cannot be determined in the simulation. It is thus not possible to compare the mostly mesoscale GWs observed during SpreadFEx (which could be responsible for seeding bubbles). It is conceivable, however, that these large-scale thermospheric and ionospheric perturbations may precondition the onset of bubbles at times after PRE or in the absence of PRE. For example, *Takahashi et al.* [2009] reported bubble formation starting at 2230 UT and 24 on 1 October (the day of this simulation). Although this simulation does not reproduce any bubbles, it is interesting to note from Figure 1 that the introduction of the body forcing produces an upward perturbation of the vertical drift between 20 and 21 UT and again between 23 and 28 UT at 45°W and equator, near São Luí VHF radar (spatial pattern of the vertical drift perturbation at 25 UT can be seen in Figure 5).

[22] Some information of the large-scale ionosphere structures can be obtained from measurements by the Global Ultraviolet Imager (GUVI) onboard of the Thermosphere Ionosphere Mesosphere Energetics and Dynamics (TIMED) satellite during the SpreadFEx campaign [*Fritts et al.*, 2009]. It is difficult, however, to derive quantitative information regarding ionospheric perturbations caused by the type of waves discussed in this paper, because (1) the near sun-synchronous scan by the satellite makes it impossible to obtain temporal changes at any specific location on scales

relevant for the gravity waves discussed here; (2) the limited width of the scan (∼20° in longitude at the equator) and the non-uniform nature of the electron density distribution make it difficult to extract any coherent spatial structure of the wave with horizontal scales of 20° (∼2000 km) or more in longitude and latitude (Figure 2). We only make some heuristic comparison here by examining the GUVI 135.6 nm emission rates from the night side (ascending) of orbits 20651 and 20652, corresponding to 0012 UT and 0148 UT of day 274, orbits 20666 and 20667, corresponding to 0024 UT and 0200 UT of day 275 (equivalently 2424 UT and 2600 UT of day 274), and orbits 20681 and 20682, corresponding to 0042 UT and 0218 UT of day 276 (Figure 8). The most evident change from day 274 to 275 at both ∼0 UT and 0200 UT is the decrease of the northern branch of the peak emission rates, located between the geographic equator and 15°N (Figures 8a and 8b). The southern branch and the emission between the two peaks (5–20°S), on the other hand, show signs of increase. This is seen also in the profile of emission rate along the satellite track, obtained by averaging over each disk scan (Figures 8d and 8e). These changes are qualitatively consistent with the large-scale ionospheric plasma density perturbations in our simulation, caused by secondary gravity waves, as seen in TEC change (Figure 2) and Nmf2 (not shown) at similar times and locations. It should be noted that the trend of some of these changes continue to day 276, especially for ∼0200 UT, and the emission rates between 5°N and 20°N at ∼ 0UT are similar for day 275 and 276. Given the large day-to-day variability of the ionospheric density and thermospheric tides, as well as the shift in location and local time of satellite tracks, it is difficult to draw any definite conclusion from such heuristic comparisons, apart from that the simulation results are not inconsistent with the observations. It should be emphasized that only the effects of perturbations associated with the parameterized body forcing are simulated by TIME-GCM. Neither the primary gravity waves nor their effects are resolvable by TIME-GCM with the current resolution.

[23] The simulation results here may also provide a plausible mechanism to explain the large amplitude perturbations of plasma drift and density observed by Communications/ Navigation Outage Forecasting System (C/NOFS) at nighttime under extreme solar minimum conditions, which have spatial scales of 500–1000 km [*Pfaff et al.*, 2010]. The C/NOFS observations show a lack of phase consistency between the perturbations of plasma drift and density. As pointed out in our analysis, this is probably because the neutral wind advection along the field lines contributes significantly to the total plasma (as well as the time-integrated effect of advection).

[24] These preliminary and qualitative comparisons with existing observations are encouraging. Extensive comparisons, however, are beyond the scope of the current study, because the main goal of the current work is to examine neutral-ion coupling processes likely associated with dissipation of convectively generated gravity waves. Direct, quantitative comparison is difficult at this point because a significant portion of the wave spectrum is missing in the numerical simulation, limited by model resolutions. Comparisons on large-scales are also challenging because of the lack of information on short-term changes on such scales from satellite observations for the campaign period. It is also noted that the analysis of the plasma density change in this work focuses on the transport. Photochemical processes, although ignored here, may still be important especially at daytime. This may be particularly important when studying the impact of globally distributed GWs.

5. Conclusions

[25] The analysis of the numerical model results demonstrates that the fluid perturbations created from the body forces generated by the dissipation of primary GWs from deep convection can cause large-scale ionospheric perturbations, including plasma density and plasma drift. These fluid perturbations include both secondary GWs and large-scale circulation cells. These secondary GWs propagate globally and encompass both E and F regions. Additionally, the circulation cells extend from 130 to 375 km, although their amplitudes decrease significantly with height above 220 km. Thus, the large neutral wind perturbations associated with these GWs and cells affect the E and F region wind dynamo and thus lead to perturbations in the plasma drifts. With the body forces calculated by the ray-tracing model and on scales resolvable by the TIME-GCM, the waves change the vertical plasma drifts by $\sim$10 ms^{-1}. Near local dusk, such changes can either enhance or weaken the pre-reversal enhancement (PRE) near the magnetic equator. Due to the persistence of tropospheric convection and the propagation of the GWs in longitude (and therefore in local time), the plasma drift perturbations last well after dusk up until midnight. Therefore, these upward vertical drifts could modulate the seeding of equatorial plasma bubbles well after sunset. The changes of the wind-driven currents are found to be very dynamic and can maximize either in the E region or F region, depending on the magnitudes of the wind perturbations, the electric conductivities, and their perturbations. The GWs also modulate the plasma transport and thus the plasma density and conductivities, with the largest contribution from advection by the neutral winds along the field lines and the plasma drifts, and somewhat smaller contribution from ambipolar diffusion. Given the significant role of the PRE and vertical plasma drift in the F-region irregularity and the ubiquitous presence of tropospheric convection, these GW-induced perturbations may have important implications for either directly triggering or preconditioning the onset irregularity. The irregularity, however, cannot be resolved by TIME-GCM due to its coarse resolution.

[26] **Acknowledgments.** We would like to acknowledge A.D. Richmond and Yongliang Zhang for their valuable comments. We also thank G. Occhipinti and an anonymous reviewer for their constructive comments. S.L.V. was supported by NASA contracts NNH07CC81C and NNH10CC98C. H.L.L. was supported by NASA contracts NNH07CC81C, NNH10CC98C, and NNX09AJ83G and by NSF CEDAR Grant No. AGS-1138784. The National Center for Atmospheric Research is sponsored by the National Science Foundation.

[27] Robert Lysak thanks the reviewers for their assistance in evaluating this paper.

References

Abdu, M. A., E. A. Kherani, I. S. Batista, E. R. de Paula, D. C. Fritts, and J. H. A. Sobral (2009), Gravity wave initiation of equatorial spread F/plasma bubble irregularities based on observational data from the SpreadFEx campaign, *Ann. Geophys.*, *27*, 2607–2622.

Anderson, D. N., B. Reinisch, C. E. Valladares, J. Chau, and O. Veliz (2004), Forecasting the occurrence of ionospheric scintillation activity in

the equatorial ionosphere on day-to-day basis, *J. Atmos. Sol. Terr. Phys.*, *66*, 1567–1572.

Artru, J., V. Ducic, H. Kanamori, P. Lognonné, and M. Murakami (2005), Ionospheric detection of gravity waves induced by tsunamis, *Geophys. J. Int.*, *160*, 840–848.

Bruinsma, S. L., and J. M. Forbes (2008), Medium to large-scale density variability as observed by CHAMP, *Space Weather*, *6*, S08002, doi:10.1029/2008SW000411.

DasGupta, A., A. Das, D. Hui, K. K. Bandyopadhyay, and M. R. Sivaraman (2006), Ionospheric perturbation observed by the GPS following the December 26th, 2004 Sumatra-Andaman earthquake, *Earth Planets Space*, *35*, 929–959.

Fejer, B. G., L. Scherliess, and E. R. de Paula (1999), Effects of the vertical plasma drift velocity on the generation and evolution of equatorial spread F, *J. Geophys. Res.*, *104*, 19,859–19,869.

Fritts, D. C., and M. J. Alexander (2003), Gravity wave dynamics and effects in the middle atmosphere, *Rev. Geophys.*, *41*, 1003, doi:10.1029/2001RG000106.

Fritts, D. C., et al. (2009), Overview and summary of the Spread F Experiment (SpreadFEx), *Ann. Geophys.*, *27*, 2141–2155.

Hocke, K., and K. Schlegel (1996), A review of atmospheric gravity waves and traveling ionospheric disturbances, *Ann. Geophys.*, *14*, 917–940.

Kherani, E. A., M. A. Abdu, E. R. de Paula, D. C. Fritts, J. H. A. Sobral, and F. C. de Meneses Jr. (2009), The impact of gravity waves rising from convection in the lower atmosphere on the generation and nonlinear evolution of equatorial bubble, *Ann. Geophys.*, *27*, 1657–1668.

Klostermeyer, J. (1972), Numerical calculation of gravity wave propagation in a realistic thermosphere, *J. Atmos. Terr. Phys.*, *34*, 765–774.

Lindzen, R. S. (1981), Turbulence and stress owing to gravity wave and tidal breakdown, *J. Geophys. Res.*, *86*, 9707–9714.

Liu, J. Y., K. M. Tsai, Y. Chen, H. Tsai, C. Lin, M. Kamogawa, and C. Lee (2006a), Ionospheric GPS total electron content (TEC) disturbances triggered by the 26 December 2004 Indian Ocean tsunami, *J. Geophys. Res.*, *33*, A05303, doi:10.1029/2005JA011200.

Liu, J. Y., Y. B. Tsai, S. W. Chen, C. P. Lee, Y. C. Chen, H. Y. Yen, W. Y. Chang, and C. Liu (2006b), Giant ionospheric distrubances excited by the M9.3 Sumatra earthquake of 26 December 2004, *Geophys. Res. Lett.*, *33*, L02103, doi:10.1029/2005GL023963.

Lognonné, P., et al. (2006), Ground based GPS imaging of ionospheric post-seismic signal, *Planet. Space Sci.*, *59*, 528–540.

Occhipinti, G., P. Lognonné, E. A. Kherani, and H. Hébert (2006), Three dimensional waveform modeling of ionospheric signature induced by the 2004 Sumatra tsunami, *Geophys. Res. Lett.*, *33*, L20104, doi:10.1029/2006GL026865.

Occhipinti, G., P. Coisson, J. Makela, S. Allgeyer, A. Kherani, H. Hébert, and P. Lognonné (2011), Three-dimensional numerical modeling of tsunami-related internal gravity waves in the Hawaiian atmosphere, *Earth Plants Space*, *63*, 847–851.

Pfaff, R., D. Rowland, H. Freudenreich, K. Bromund, G. Le, M. Acuña, J. Klenzing, C. Liebrecht, and S. Martin (2010), Observations of DC electric fields in the low latitude ionosphere and their variations with local time, longitude, and plasma density during extreme solar minimum, *J. Geophys. Res.115,* A12324, doi:10.1029/2010JA016023.

Richmond, A. D. (1978), Gravity wave generation, propagation and dissipation in the thermosphere, *J. Geophys. Res.*, *83*, 4131–4145.

Richmond, A. D., E. C. Ridley, and R. G. Roble (1992), A thermosphere/ionosphere general circulation model with coupled electrodynamics, *Geophys. Res. Lett.*, *19*, 601–604.

Roble, R. G. (1995), Energetics of the mesosphere and thermosphere, in *The Upper Mesosphere and Lower Thermosphere: A Review of Experiment and Theory*, edited by R.M. Johnson, and T.L. Killeen, no. 87 in Geophysical Monograph Series, p. 356, Americal Geophysical Union, Washington, D.C.

Roble, R. G. (2000), On the feasibility of developing a global atmospheric model extending from the ground to the exosphere, in *Atmospheric Science Across the Stratopause*, edited by D.E. Siskind, S.D. Eckermann, and M.E. Summers, no. 123 in Geophysical Monograph Series, p. 342, Americal Geophysical Union, Washington, D.C.

Roble, R. G., and E. C. Ridley (1994), A thermosphere-ionosphere-mesosphere-electrodynamics general circulation model (TIME-GCM): Equinox solar cycle minimum simulations (30–500 km), *Geophys. Res. Lett.*, *21*, 417–420.

Takahashi, H. et al. (2009), Simultaneous observation of ionospheric plasma bubbles and mesospheric gravity waves during the SpreadFEx Campaign, *Ann. Geophys.*, *27*, 1477–1487.

Vadas, S. L. (2007), Horizontal and vertical propagation and dissipation of gravity waves in the thermosphere from lower atmospheric and thermospheric sources, *J. Geophys. Res.*, *112*, 06405, doi:10.1029/2006JA011845.

Vadas, S. L., and G. Crowley (2010), Sources of the traveling ionospheric disturbances observed by the ionospheric TIDDBIT sounder near Wallops Island on October 30, 2007, *J. Geophys. Res.*, *115*, A07324, doi:10.1029/2009JA015053.

Vadas, S. L., and D. C. Fritts (2001), Gravity wave radiation and mean responses to local body forces in the atmosphere, *J. Atmos. Sci.*, *58*, 2249–2279.

Vadas, S. L., and D. C. Fritts (2009), Reconstruction of the gravity wave field from convective plumes via ray tracing, *Ann. Geophys.*, *27*, 147–177.

Vadas, S. L., and H.-L. Liu (2009), Generation of large-scale gravity waves and neutral winds in the thermosphere from the dissipation of convectively generated gravity waves, *J. Geophys. Res.*, *114*, A10310, doi:10.1029/2009JA014108.

Vadas, S. L., and H.-L. Liu (2013), The large-scale neutral and plasma responses to the body forces created by the dissipation of gravity waves from 6 hours of deep convection in Brazil, *J. Geophys. Res. 118*, doi:10.1002/jgra.50249.